Insights into the stability and reactivity of lithiated Si-binder interfaces for next generation lithium-ion batteries

Rita Maji [a,*], Michele A. Salvador [b], Alice Ruini [b,c,d], Rita Magri [b,c,d], Omer Suat Taskin [e,f], Neslihan Yuca [f,g], Elena Degoli [h,c,d]

[a] Dipartimento di Scienze e Metodi dell'Ingegneria, Università di Modena e Reggio Emilia, Via Amendola 2, Padiglione Tamburini, I-42122 Reggio Emilia, Italy
[b] Dipartimento di Scienze Fisiche, Informatiche e Matematiche sede ex-Fisica, Università di Modena e Reggio Emilia, Via Campi 213/A, 41125 Modena, Italy
[c] Centro S3, Istituto Nanoscienze-Consiglio Nazionale delle Ricerche (CNR-NANO), Via Campi 213/A, 41125 Modena, Italy
[d] Centro Interdipartimentale di Ricerca e per i Servizi nel settore della produzione, stoccaggio ed utilizzo dell'Idrogeno H2–MO.RE., Via Università 4, 41121 Modena, Italy
[e] Istanbul Univ, Inst Marine Sci & Management, Dept Chem Oceanog, TR-34134 Istanbul, Turkiye
[f] Enwair Energy Technol Corp, TR-34469 Maslak, Istanbul, Turkiye
[g] Istanbul Tech Univ, Energy Inst, TR-34169 Maslak, Istanbul, Turkiye
[h] Dipartimento di Scienze e Metodi dell'Ingegneria, Università di Modena e Reggio Emilia and Centro Interdipartimentale En&Tech, Via Amendola 2, Padiglione Morselli, I-42122 Reggio Emilia, Italy

HIGHLIGHTS

- Adhesion of co-binders to new active material surfaces.
- Influence of lithiation on the optimal polymer/active material interface geometry.
- Atomistic knowledge of binding to optimize the properties of Si/binder interfaces.

ARTICLE INFO

ABSTRACT

We explore, through a first principle approach based on density functional theory, lithiated-silicon (Li-Si) surfaces and their intricate interactions with binders in lithium-ion batteries. A meticulous analysis of Li insertion in the Si-subsurface layer unveils crucial dynamics, including surface reconstructions, and structural changes in different Si facets (Si-110 and Si-111). The impact of lithium content and Si facet orientation on the binder adhesion strength demonstrates that increasing the number of subsurface Li atoms weakens adhesion. However, a strategic co-binding approach, in which polyvinyl alcohol (PVA) is associated with polyaniline (PANI), polyaniline functionalized PANI with boronic acid groups (B-OH_PANI) or polyvinylidene fluoride (β-PVDF), is revealed to be a decisive factor in stabilizing monomers on the surface. Advanced electronic structure analyses portray changes in the charge density distribution and electronic states due to Li insertion into the Si surfaces. Molecular dynamics simulations of bulk co-binder models provide a concrete visualization of the structural relaxations and bonding interactions at the Li-Si/co-binder interface. The insights derived from this study serve as a foundation for the design and development of cutting-edge lithium-ion battery materials.

1. Introduction

Efficient lithium-ion batteries with silicon anodes represent a major goal in battery technology. Silicon (Si) is an attractive material for battery anodes because of its high theoretical capacity, and faster charging, which makes Si-based Li-Ion Batteries (LiBs) very promising for electric vehicles and other applications where high energy density is required [1–3]. However, there are several key challenges and considerations when using silicon anodes in lithium-ion batteries: volume expansion that leads to cracks, degradation of cyclability, and most importantly, safety concerns as silicon is more reactive than graphite [4,5].

Researchers have been actively working to address the practical challenges of developing Si-based LiBs in recent years. New Si-based electrode materials, such as nanostructured Si, Si nanoparticles, and

Si-graphene composites are being explored since these materials aim to mitigate the issues related to volume expansion and contraction during charge and discharge cycles [2,3,5,6]. Additionally, to accommodate the volume expansion of Si, polymeric binders are added in the manufacture of the battery's electrodes. Binders are polymeric materials that hold together the active electrode particles, improving the adhesion to the current collectors, typically made of aluminum for the cathode and copper for the anode. The key functions of binders in LiBs are driving the choice of the optimized binder for the specific requirements and the intended application: the proper formulation of suitable compositional varieties is an active area of research. Another key feature, essential for battery performance and safety, is maintaining a stable Solid Electrolyte Interphase layer (SEI) [7,8]. The SEI forms when the lithium ions in the electrolyte react with the surface of the electrode. This reaction is irreversible, so the SEI will continue to grow over time.

The major components of the SEI on a lithium-ion battery are a mixture of lithium compounds, such as lithium oxide (Li_2O), lithium carbonate (Li_2CO_3), and lithium fluoride (LiF). These compounds are formed when the lithium ions in the commonly used electrolytes react with the surface of the anode during the first charge cycle. The SEI also contains organic compounds, such as lithium ethylene dicarbonate (LEDC) and lithium dibutyl phosphate (LiDBP) [9–11]. These compounds are formed from the decomposition of the electrolyte solvent and other additives. In conclusion, the thickness and composition of the SEI can vary depending on the type of electrode material, the composition of the electrolyte, and the charging conditions [12,13]. As SEI is a critical component of lithium-ion batteries, researchers are actively working to develop new methods for engineering the SEI. Moreover, the modeling of SEI is related to the multi-component effect, where the interaction of Li with the battery components plays an important role [14,15].

Mostly, recent efforts are devoted to developing new silicon-based electrode materials that have the potential to deliver a much higher energy density than traditional graphite-based electrode materials and to design safer electrolytes with new solid-state electrolytes that are less flammable and more resistant to thermal runaway than traditional liquid electrolytes [9,14,16–18]. Here a common issue is the interaction of Li with the other battery components. Moreover, the impact of the lithiation/de-lithiation processes on structural degradation is one important focus of recent studies, as they are related to mechanical stability. Therefore, by understanding the interaction of Li with the battery components, researchers can develop new battery architectures that can mitigate the current challenges. In this aspect, atomistic simulations can facilitate such understanding, which is relatively limited [19,20].

Generally, self-healing binders utilize intrinsic or extrinsic mechanisms to restore functionality. In this paper, we focus on recently proposed functionalized molecules where boronic acid ($-B(OH)_2$) groups are bonded to aniline units in the polymer backbone (B–OH_PANI) [21–23]; such binders were considered by themselves or in a co-polymer model with poly[vinyl alcohol] (PVA) [23]. The primary reason for the use of PANI-based polymers is to increase the electrical conductivity of the electrode in addition to its binding property. Boronic acid-functionalized PANI deploys a self-healing ability to the structure. We also explored a co-polymer model of PVA with Polyaniline (PANI) or Polyvinylidene fluoride (PVDF), two most commonly used polymer binders that lack inherent self-healing functionality [24,25]. The adhesion properties of a Si anode are related to the combined effect of the surface morphology and the type of polymeric binders. Moreover, for its potential application on next-generation LiBs, the impact of introducing Li in Si, on the surface adhesion properties needs to be explored. First-principles calculations can provide insight into the atomic scale structure with related electronic properties, the binding mechanism, and its correlation with the optimal anode-binder interface geometry. The interface structure is influenced by several factors and its detailed characterization is necessary: moreover, an atomistic knowledge of the binding mechanisms can help to tailor and optimize the properties of the interfaces.

In this article, we discuss the impact of different contents of Li atoms, inserted in the Si anode, on the binding mechanisms of B–OH_PANI, PVA, PANI, and β-PVDF co-polymers considering two differently oriented Si surfaces. The calculation details, the lithiated Si-slab, and co-binder structures are described in Section 2. The results obtained for different Li sub-surface content and structurally optimized binding geometries with consequent monomer/surface modifications are discussed in Sections 3.1 and 3.2. In Section 3.3 we analyze the electronic properties and charge transfers relevant to the binding mechanisms to the lithiated Si surfaces. We shed some light on the role of the different surface orientations and the co-binding properties at different Li content. As a more realistic model of the anode-binder interface, we modeled the bulk structure of the co-polymers PVA+PANI, PVA+B–OH_PANI, and PVA+β-PVDF in a Li–Si bilayer periodic model discussed in Section 3.4. Finally, in Section 4 our conclusions and future perspectives are reported.

2. Methodology

To investigate the impact of the inclusion of Li on the adhesion properties of different polymeric binders [SM: Figure 1S] to Si-based anodes, we modeled the surfaces using Si-slabs. To better extract the role of Li on the interface properties we restricted the Li insertion to the interstitial layer just below the outmost Si atomic layer. Two different surface terminations, Si-110 and Si-111, were considered. We have chosen for the two orientations clean and unreconstructed surfaces that have dangling bonds differently oriented. The optimized cell dimensions of Si-110 and Si-111 are 19.319 Å × 21.72 Å × 26.39 Å and 19.19 Å × 19.95 Å × 30.81 Å, respectively. To model the lithiated surfaces, we consider different numbers of Li atoms inserted between the first two subsurface Si layers of the slab as depicted in Fig. 1. For each number of Li atoms, three different initial configurations of Li insertion have been checked to optimize the Li positions in the Si matrix. Next, the lowest energy configurations have been optimized further for the final analysis as explained below. The binder unit adsorption and interface formation are examined on the lithiated surface side of the slab whereas the other side (bottom layer) is fully passivated using H atoms.

First-principles calculations were performed using the Quantum Espresso [26] package, with a plane wave-based implementation of density functional theory (DFT). The screened ionic potentials are approximated by *norm conserving* pseudopotentials [27]. The exchange–correlation contribution to the total energy is estimated using a gradient-corrected Perdew–Burke–Ernzerhof (PBE) [28] functional. Minimum energy configurations for different numbers of Li on sub-surface Si-layers were obtained using a variable cell relaxation scheme [SM: Figure 2S]. Next, starting from the optimized lithiated surfaces, minimum energy structures with monomers were obtained in the super-cell using the BFGS [29] minimization scheme of total energies. We used a 800 eV plane wave energy cutoff and a $3 \times 3 \times 1$ k-mesh. The geometry optimization was iterated until the forces were less than 10^{-3} Rydberg/Bohr for all atoms. During the structural optimization, the bottom layers of the slabs were kept fixed. For the calculation of the density of states of the optimized geometries, we used a $8 \times 8 \times 1$ k-mesh. For all configurations, the Van der Waals interaction was included through the vdW-DFT module [30]. We also checked different possible orientations of the binders on the lithiated surface following the same approach as our recent work [23].

Classical molecular dynamics (MD) calculations as implemented in the Gromacs software [31] were used to generate equilibrated structures combining different polymer units. From these equilibrated structures, we cut a small portion to be used as input for the quantum DFT calculations. The size and the properties of the bulk systems obtained from MD, and the characteristics of the portion used in DFT will be

described in the results Section 3.4. This strategy was used to start from a reasonably stable configuration for the polymeric ensemble instead of a random aggregate which would have been far away from an equilibrium structure. To perform the MD calculations, each molecule (PANI, B–OH_PANI, PVA, and β-PVDF) was previously optimized in the gas phase, using localized-base DFT calculations as implemented in the Orca software [32,33] at the B3LYP/6-311g [34,35] level of theory, including D3BJ empirical dispersion correction [36,37]. The vibrational frequency calculations ensured that the obtained structures correspond to minima in the potential energy surface, and partial charges were calculated with the ChelpG scheme [38]. For the MD simulations, cubic boxes were created with the molecules placed randomly using Gromacs pre-processing tools. Except for the parameters which include the boronic acid group in PANI, we used OPLS-AA force field parameters [39] available in Gromacs software. For the boronic acid group, we used the parameters obtained by Kurt and co-workers [40], converted from AMBER to OPLS-AA force field.

We performed a minimization step using the steepest descent algorithm, followed by an initial equilibration step using a leapfrog [41] algorithm in an NPT ensemble at temperature (T) 300 K and pressure (P) 1 bar. In this first step, the temperature was kept constant using a velocity-rescaling thermostat [42], and pressure was controlled by Berendsen barostat [43]. The system was heated up to 600 K and then cooled down to 300 K in a NPT ensemble, followed by a second equilibration cycle, consisting of one NPT and one NVT run, at the same temperature. In this second NPT run, we used the Parrinello-Rahman barostat [44], and the velocity-rescaling thermostat was used both in the NPT and NVT steps. This equilibration protocol was followed by the production phase, where we collected and analyzed properties such as density and pair correlation functions (g(r)).

From the experimental point of view, the feasibility of the Boronic acid doped PANI-PVA binders has been demonstrated and samples have been indeed synthesized as explained in the SM; the performance of the final cells was also analyzed, as shown in SM [SM: Figure 3S].

3. Results and discussions

3.1. Li on Si-subsurface layer

The insertion of Li atoms below the outmost Si surface layer forms different local coordination for the Si atoms in the Si-110 and Si-111 facets. The formation energy [45] (E_f) of different Li inserted structures are calculated as

$$E_f = E_{slab+Li} - E_{slab} - n_{Li}E_{Li} \qquad (1)$$

where $E_{slab+Li}$ and E_{slab} are the total energies of the optimized Si-slabs with and without lithium ions inserted into the silicon slab. We considered 8, 16, and 24 Li atoms in Si-110, corresponding to a cell containing 320 Si atoms, and 10, 20, and 30 Li atoms for Si-111, the cell containing 360 Si atoms. E_{Li} is the energy of a Li atom calculated from Li-bulk, and n_{Li} is the number of Li atoms.

Fig. 1(g) describes how the formation energy changes during lithium insertion into the silicon slabs. The negative formation energy indicates that lithium insertion is energetically favorable. A lower formation energy suggests a more stable configuration. The formation energy typically decreases (becomes more negative) as more Li atoms are introduced, indicating that the system becomes more stable with an increasing lithium content. It depends on Si facet orientation in agreement with the lithiation anisotropy explored in Ref. [45]. However here due to the low Li content, the overall difference in formation energy between the two orientations is relatively small. The behavior of Li within a Si matrix depends on several factors, including the crystal facet, defects, and the specific conditions of the battery system. In our case, since the surfaces are clean, Li insertion on the Si-facet is mainly influenced by the structural reconstruction and local environment. For Si-110 [Fig. 1(a–c)], with 8 Li, the optimized geometry leads to

elongated Si–Si bonds (2.43 Å) nearest to the Li sites, without impacting much all other surface Si atoms. Whereas, for 24 Li, the need to accommodate them requires more Si–Si bonds closest to the Li atoms getting elongated (2.40–2.44 Å) [SM: Figure 4S]. In all cases, most of the Li is positioned such that it is surrounded by six Si atoms with Li–Si distances of approximately 2.48–2.68 Å. These bond lengths are similar to those found for interstitial Li in layered Si [46] but differ from those found for the inclusion of Li in crystalline Si [47].

For Si-111, even with a small number of inserted Li atoms (10 Li atoms) [Fig. 1(d)], the Si–Si bonds at the surface are mostly elongated (2.39–2.42 Å) and Li is situated within six neighbor Si atoms alike Si-110, with Li–Si distances ~2.48–2.78 Å Moreover, with the increasing number of Li (20 and 30 Li atoms), the (111) facet [Fig. 1(e, f)] undergoes a surface reconstruction, that impacts the stability and reactivity, as is also evident from the formation energy variation [Fig. 1(g)]. For 30 Li atoms, there are Li atoms in proximity (Li–Li distance = 2.46 Å). The inserted Li exhibits a varying coordination number, different from that of the configurations with less Li content, resulting in Li–Si distances ~3 Å [SM: Figure 5S]. This supports the distortion of the Si network upon lithiation and formation of different Si–Li alloys found in previous works [48]. Understanding the nature of these reconstructions is important for predicting the behavior towards the binding mechanism, which will be explored in detail from electronic structure analysis in Section 3.3. Although our supercell model includes a vacuum, to identify the volume expansion as a function of lithium content a relative volume is calculated as the volume of the lithiated configurations divided by the volume of pristine Si. For all the Li content considered in this analysis, relative volume expansion is of the order of 1.002–1.01, as expected for the low level of Li insertion.
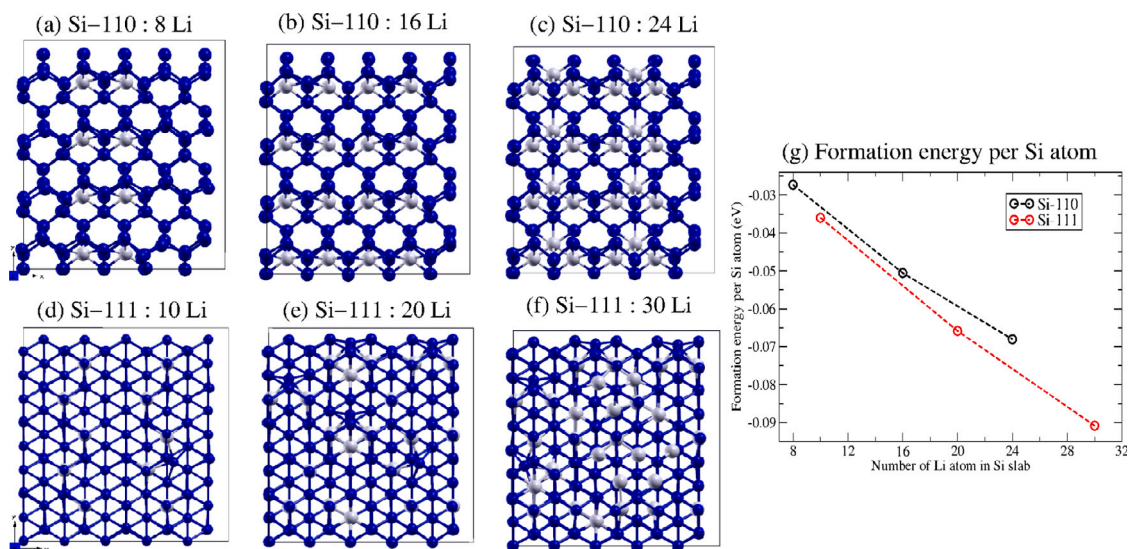
3.2. Binders at lithiated Si-surfaces

The adsorption of binders on lithiated silicon (Li–Si) surfaces is an important aspect, especially when dealing with high-capacity materials like silicon, which undergo significant volume changes during cycling. The interaction between binders and the electrode's surface, especially in the presence of lithium ions, is a critical consideration.

The adsorption energy (E_A) of the binder is calculated as

$$E_A = E_{Li\text{-}Si+X+Y} - E_{Li\text{-}Si} - n_X E_X - n_Y E_Y. \qquad (2)$$

X, Y are the adsorbed monomers, in our case X: PVA, PANI, β-PVDF, B–OH_PANI, and co-polymer X+Y: PVA + PANI, PVA + B–OH_PANI, and PVA + β-PVDF structures. $E_{Li\text{-}Si+X+Y}$ and $E_{Li\text{-}Si}$ are the total energies of the optimized Li inserted Si-slabs with the monomer or co-binder and the bare Li inserted Si-110/111, respectively. E_X/E_Y is the total energy of the isolated binder calculated within the same supercell, and n_X, n_Y is the number of monomers. In the case of co-binding the energies of both the isolated monomers X and Y are considered in the equation, otherwise $n_Y = 0$.

Table 1

Adsorption energy (E_A) of PVA, PANI, β-PVDF, B–OH_PANI, and co-binder combinations on the Lithiated Si-110 slabs. The values are reported only for the lowest energy structures.

X	E_A (eV): 8 Li	: 16 Li	: 24 Li
PVA	−1.611	−1.705	−1.681
PANI	−1.332	−1.297	−1.205
β-PVDF	−1.055	−0.994	−0.980
B–OH_PANI	−1.806	−1.160	−2.840
One PVA + One PANI	−4.375	−4.002	−2.354
One PVA + One β-PVDF	−3.950	−3.557	−2.947
One PVA + One B–OH_PANI	−3.390	−3.249	−2.470

Fig. 1. Optimized Si surfaces (x–y plane) with a different number of Li atoms: upper panel for Si-110 (a) 8 Li, (b) 16 Li, and (c) 24 Li. Lower panel for Si-111 with (d) 10 Li, (e) 20 Li, and (f) 30 Li atoms. (g) Formation energy plot for different numbers of Li atoms inserted in Si-110 and Si-111 surfaces. Si and Li atoms are presented with blue and gray color balls respectively. (For interpretation of the references to color in this figure legend, the reader is referred to the web version of this article.)
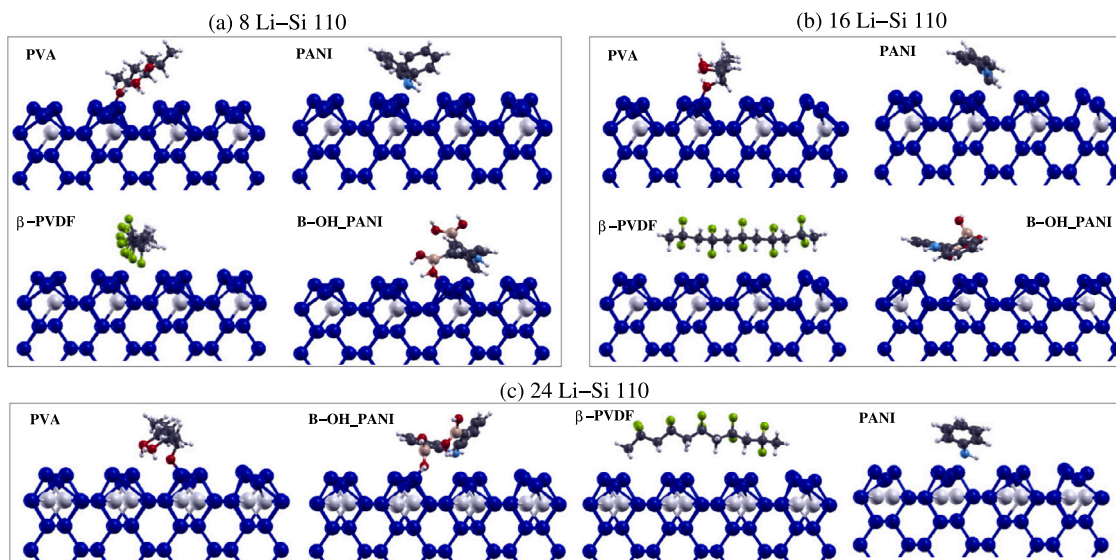
Fig. 2. Optimized Li–Si-110 surface with binders for different Li content (a) 8 Li, (b) 16 Li, and (c) 24 Li. Binders are marked accordingly. Si and Li atoms are presented with blue and gray balls respectively. (For interpretation of the references to color in this figure legend, the reader is referred to the web version of this article.)

3.2.1. Lithiated Si-110 surface

Starting from the Si-110 surface 8, 16, and 24 Li atoms were inserted and the surfaces were optimized following the procedure discussed in the method section and flowchart in SM: Figure 2S. The optimized configuration with one monomer of PVA, PANI, B–OH_PANI, and β-PVDF at different lithiated surfaces adsorb differently as evident from Fig. 2. All the corresponding adsorption energy values [using Eq. (2)] are listed in Table 1. The optimized configuration with one PVA monomer shows an elongated Si–O bond (1.82 Å) with the nearest unsaturated Si atom. However, with increasing the number of Li atoms (such as 24 Li), the availability of Si sites and the chemical environment of unsaturated Si atoms changes. In this case one of the strong Si–O bonds forms (1.68 Å) and the H of the –OH group is attached to another –OH of PVA, due to the unavailability of Si sites at neighboring positions. Therefore, the adsorption energy varies depending on the nature of anchoring and orientation of the monomer. In the case of PANI and β-PVDF [Fig. 2(a–c)], where both show physisorption on the surface, we observe that increasing Li at the Si surfaces reduces the reactivity

of the Si - binder long-range interactions as evident from lowering of adsorption energy values (Table 1). B–OH_PANI mostly orients parallel to the surface, although depending on the –B(OH)$_2$ orientation, at low Li insertion, it forms one of the stretched Si–O bonds (1.89 Å), whereas for highest Li content one strong Si–O bond (1.68 Å) forms and the detached H from –OH of –B(OH)$_2$ saturates one of the closest Si (Si–H = 1.49 Å) site [Fig. 2(c)].

For all the co-binders [Fig. 3] the overall trend of the adsorption energy [Table 1] leads to a weakening of adhesion with increasing Li content. This can be explained by the reduction of unsaturated Si at the surface due to Li insertion at the subsurface layer, evident from respective Löwdin charges of Si atoms [SM: Table 1S]. For co-binding, combinations of each monomer with PVA help to stabilize the monomer on the surface. This can be further validated by the adsorption energy values and reduction of overall distortion of the same monomers with co-binding adsorption.

The intermolecular interaction between PVA and PANI/β-PVDF/ B–OH_PANI also causes the adsorption energy to be lower than the
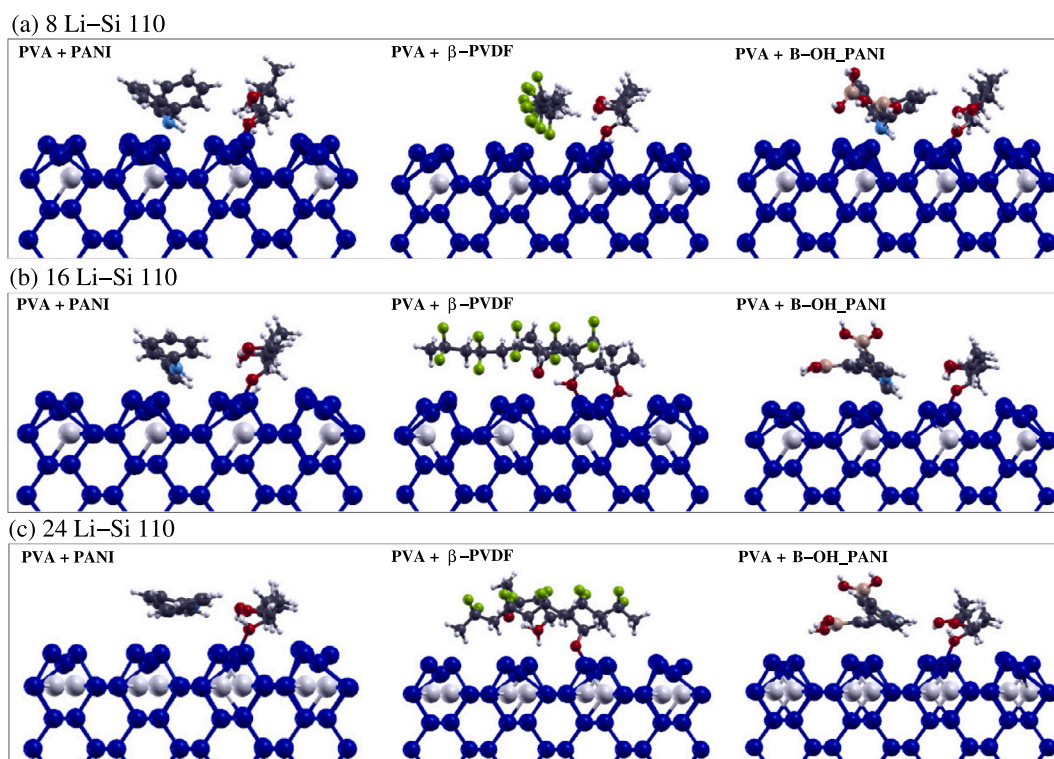
Fig. 3. Optimized Li–Si-110 surface with co-binders for different Li content (a) 8 Li, (b) 16 Li, and (c) 24 Li. Binder combination actions are marked accordingly. Si and Li atoms are presented with blue and gray balls respectively. (For interpretation of the references to color in this figure legend, the reader is referred to the web version of this article.)

Table 2
Adsorption energy (E_A) of PVA, PANI, β-PVDF, B–OH_PANI, and co-binder combinations to the Si-111 slabs. The values are reported only for the lowest energy structures.

X	E_A (eV): 10 Li	: 20 Li	: 30 Li
PVA	−2.343	−2.109	−0.560
PANI	−1.619	−0.877	−0.765
β-PVDF	−1.266	−1.147	−0.964
B–OH_PANI	−2.032	−1.801	−1.106
One PVA + One PANI	−4.191	−1.968	−2.194
One PVA + One β-PVDF	−4.488	−3.813	−2.558
One PVA + One B–OH_PANI	−5.351	−2.797	−1.973

sum of the adsorption energies of the two single monomers [Table 1]. The interaction between PVA and β-PVDFs involves hydrogen bonding between the hydroxyl groups/C–H of PVA and the fluorine atoms of β-PVDF, as evident from the optimized configurations with the minimum F–H distance 2.4 Å for F···H–O and 2.3–2.8 Å for F···H–C respectively for different Li–Si-110 configurations. Moreover, for B–OH_PANI, the adsorption configuration for the co-binder case is different than the one with a single monomer, as we started with the optimized geometry with PVA and the final optimized structure of the co-binder finds a lower number of available Si sites.

3.2.2. Lithiated Si-111 surface

For Si-111 surface with insertion of 10, 20, and 30 Li atoms three optimized [Section 2 & SM: Figure 2S] Li–Si surfaces were generated respectively. The optimized configurations with a single monomer of PVA, PANI, β-PVDF, and B–OH_PANI at different Li–Si surfaces are shown in Fig. 4. The adsorption energies [using Eq. (2)] for all configurations with different monomers on the Si-slab are listed in Table 2. For Li content 10 and 20, the adsorption of one PVA monomer is associated with the formation of strong Si–O bonds, 1.68 Å and 1.71 Å respectively. The remaining H of the adsorbed –OH group [Fig. 4(a)] saturate one of the nearest Si sites (Si–H = 1.48 Å) for low Li content, whereas for 20 Li [Fig. 4(b)], due to the unavailability of unsaturated

Si at the nearest neighbor region, it leads to over coordination of the closest –OH group in PVA. This fact leads to an enhancement of adhesion in the former case (−2.34 eV) relative to the latter adsorption configuration (−2.11 eV). For maximal Li content, one PVA monomer shows physisorption with relatively weak adhesion as evident from the structure [Fig. 4(c)] and the adsorption energy value. For PANI and β-PVDF, no such saturation or bond formation occurred irrespective of Li content. However, the reorientation of the monomer happens as a consequence of the larger exposition of the monomers to the surface [Fig. 4(a–c)]. For one B–OH_PANI, it tends to orient itself facing the –OH group to the surface, which leads to elongated Si–O bond (1.92 Å) formation for 10 and 20 Li–Si surfaces. For 30 Li no such Si–O bonds are formed, and the molecules tend to be parallel with higher surface coverage. Notably, the two –B(OH)$_2$ groups within the monomer undergo a rotational adjustment to minimize steric repulsion, a pattern consistently observed across all optimized configurations of Li–Si 110/111 interfaces. Finally, we analyze the three cases of co-binding [Fig. 5(a–c)] on the Si–111 slab. Like Li–Si-110, the overall trend of the adsorption energy [Table 2] leads to a weakening of adhesion with increasing Li content. However, for PVA + PANI the main difference between 20 and 30 Li content could be due to the intermolecular interactions as two monomers arrange themselves differently during optimizations.

For 10 Li atoms [Fig. 5(a)], the lowering in adsorption energy is instead due to the Si–O bond formation and to one H-saturated Si site. For PVA + β-PVDF in all Li–Si-111 surfaces, the overall lowering in adsorption energy is a combined effect of Si–O bond formation (1.66–1.71 Å), H saturated Si site (10 and 20 Li) and the intermolecular interactions. The interaction between PVA and β-PVDF can involve hydrogen bonding between the hydroxyl groups of PVA and the fluorine atoms of β-PVDF, as evident from optimized configurations and they are nearby (F–H distance in F···H–O being 1.8–2.0 Å) compared to Li–Si-110 configurations. In the case of PVA + B–OH_PANI the two monomers arrange themselves by establishing hydrogen bond-based interactions between them, that involve the –OH group of PVA
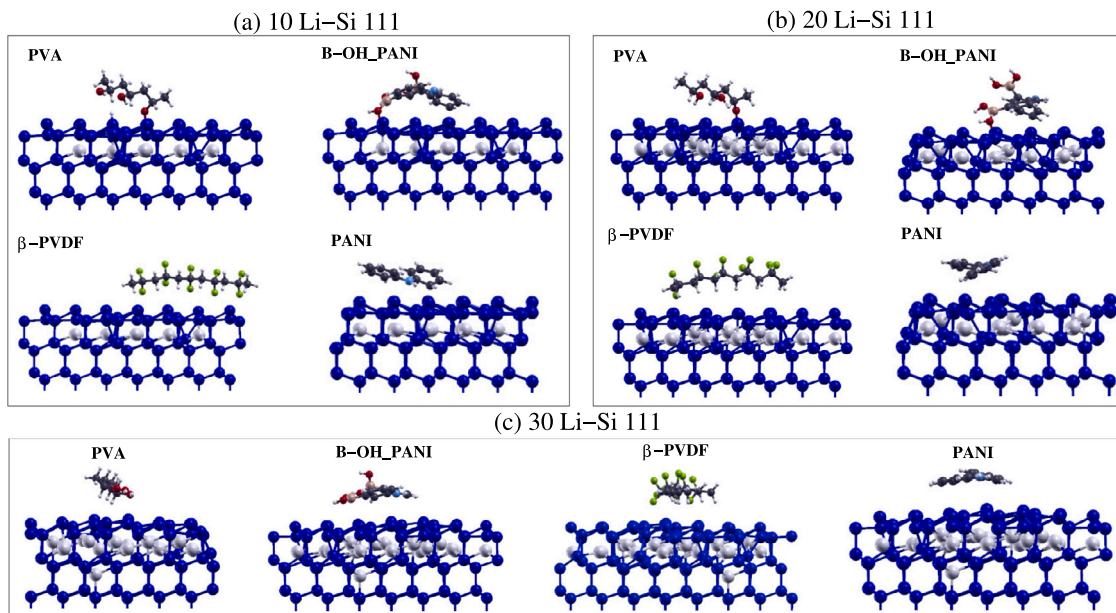
Fig. 4. Optimized Li–Si-111 surface with binders for different Li content (a) 10 Li, (b) 20 Li, and (c) 30 Li. Binders are marked accordingly. Si and Li atoms are presented with blue and gray balls respectively. (For interpretation of the references to color in this figure legend, the reader is referred to the web version of this article.)
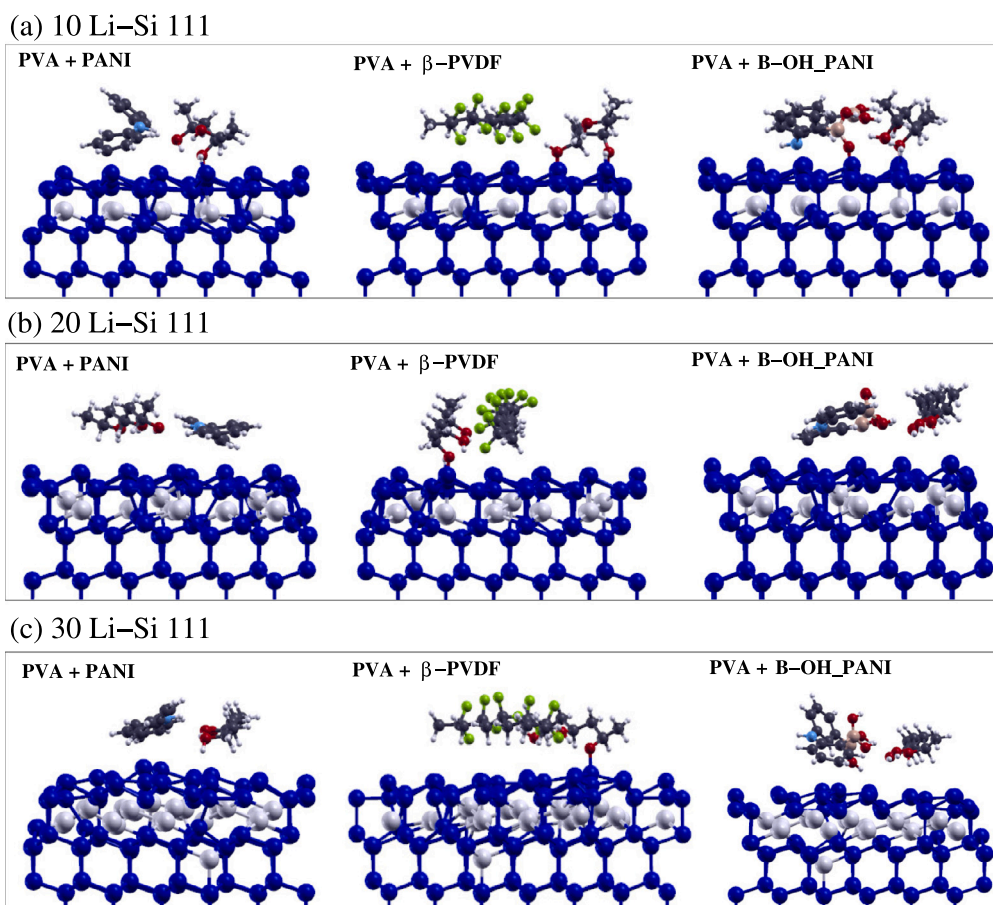

Fig. 5. Optimized Li–Si-111 surface with co-binders for different Li content (a) 10 Li, (b) 20 Li, and (c) 30 Li. Binder combination actions are marked accordingly. Si and Li atoms are presented with blue and gray balls respectively. (For interpretation of the references to color in this figure legend, the reader is referred to the web version of this article.)

and –B(OH)$_2$ group of functionalized PANI, which is different than Li–Si-110 surfaces.

From the adsorption energy values, [Tables 1, 2], it is evident that the adhesion of these polymeric monomers is stronger for Li–Si-111 than for Li–Si-110, due to Si passivation/saturation effects, a combined impact from inserted Li and adsorption of binder(s). Still, we must notice that co-binding is preferred and this is reflected by the energy gained by the addition of the second binder. However, we can still remark that the increasing number of Li impacts the adsorbent reactivity by weakening the adhesion irrespective of the Si facet orientation and co-binder composition.

3.3. Electronic properties of Li–Si & co-binder interfaces

We find that the adhesion of the binders is enhanced by the co-binding approach. The adsorption of PVA and another monomer is more favorable than the adsorption of two monomers of a similar kind, irrespective of the Si facet type [23].

Therefore for a detailed analysis of the electronic structure, we focus on the charge densities and projected density of states of three of the co-binder configurations PVA + PANI, PVA + β-PVDF, and, PVA + B–OH_PANI for the medium Li content, that is 16 Li–Si-110 and 20 Li–Si-111.

For the chemical environment of the atoms at the Li–Si interface, the charge distribution is calculated from the charge density difference as:

$$\Delta\rho = \rho(Li - Si + b) - \rho(Li - Si) - \rho(b) \qquad (3)$$

where ρ(Li–Si+b), ρ(Li–Si), and ρ(b) correspond to the charge density of the lithiated slab with co-binder, lithiated slab, and co-binder configuration, respectively. We considered only the Local Density of States (LDOS) obtained from the projection of atomic orbitals and the LDOS (p orbitals only) on the Si sites bonded or close to any of the binder elements at the Li–Si slab/binder interfaces are analyzed.

To quantify the charge transfer at the Li–Si-110 interface, the charge density difference $\Delta\rho$ is shown in Fig. 6 1(a–c). For PVA + PANI [Fig. 6 1(a)], a large charge accumulation (green isosurface) occurs at the H-saturated Si site and the Si close to C from the PANI (2.12 Å), whereas a depletion-accumulation isosurface is present along the Si–O bond meaning that some charge is transferred from Si to O in the bond formation. Weak charge accumulation (lower than the isosurface values plotted here) also occurs where H from the binder is heading towards the Si site (2.38 Å). As a result of adsorption on Li–Si-110, LDOS of the p bands [Fig. 6 1(d)] around the Fermi energy of fully/partially saturated Si are almost suppressed. The evolution of Si1 from slab to the presence of Li is due to local strain occurring as a fact of Li insertion at the subsurface layer (2.65 Å). The suppression of unsaturated Si 2(p) states is stronger in the case of Si–O and Si–H, as expected. In general, the absorption does not impact so much on the other orbitals of the binder (C, N atoms), so they are not of much interest for the interface analysis. In the case of PVA + β-PVDF [Fig. 6 1(b)], $\Delta\rho$ shows a depletion-accumulation along the elongated Si–O–H–C bond (1.81 Å), also evident from the suppression of Si-2p orbitals. Apart from this charge accumulation occurs at surface Si atoms, where H from the PVA is heading at a distance of 2.25 Å. The LDOS plot [Fig. 6 1(e)] of the Si1 site shows an interesting feature, as it evolves from slab to lithiated configurations. Here it indicates how the Li insertion at the subsurface layer can partially saturate the surface Si atoms (Si1:Li–Si no available states at Fermi energy). However, upon adsorption of the co-binder, the reorganization of the local coordination can lead to such available electronic states [Fig. 6 1(e): LDOS Si1-binder]. A similar trend of charge density difference is observed for PVA + B–OH_PANI and LDOS plots [Fig. 6 1(c, f)] shows a clear evolution of the same Si site starting from slab to the presence of Li and upon co-binder adsorption. Therefore, the same Li–Si surface responds differently for the three

co-binder adsorptions and local coordination maximally impacts the electronic structure of the Li–Si interface.

For Li–Si-111 with three co-binders [Fig. 6 2(a–c)], a similar charge density analysis is performed. The physisorption nature of PVA + PANI, [Fig. 6 2(a, d)] as discussed earlier, shows very weak charge accumulations, hence impact on LDOS from bare Li–Si to binder adsorbed surface is weak. However, Si sites from slab to lithiated surface are distinguishable. In the case of PVA + β-PVDF [Fig. 6 2(b, e)], the charge accumulation and depletion based on the nature of bonds is evident as discussed for the Li–Si-110 facet. From the LDOS plot, suppression of the Si2 peak is due to the H-saturation of that site. However, Si1 which was initially four-coordinated in the case of a bare Li–Si surface with three bond lengths equal to 2.39 Å and one compressed bond of 2.29 Å becomes an active site for adsorption due to reorganization in the presence of the binder, which is consistent with the LDOS [Fig. 6 2(e) red line]. For PVA + B–OH_PANI [Fig. 6 2(c)], it shows a charge depletion-accumulation at Si–C (2.04 Å) interfaces and a weak accumulation (not visible due to the chosen range of isosurface value) at Si2 (H–Si 2.61 Å). Si1 is still three-fold coordinated at the bare Li–Si surface, however, Si2 is partially reorganized by the Li (2.61 Å) and they are finally in the process of better passivation upon adsorption, as evident from the corresponding LDOS plot [Fig. 6 2(f) black line]. This analysis should hold for all other co-binder adsorbed configurations for different Li content in Si-110/111, which are not considered here [SM: Figure 6S & 7S]. This charge depletion-accumulation process can be further validated by comparing partial charges of any single Si site in Si-slab (3.83 e), in bare lithiated Si-slab (3.96 e) and upon co-binding adsorption (3.54 e). The reduction of unsaturated Si due to Li insertion as discussed previously can also be quantified from Löwdin charges of Si (e.g. 3.83/3.98 e) without/with Li [SM: Table 2S]. Moreover, variability on Löwdin charges of Si atoms [SM: Table 2S] was observed during different co-binding adsorption, which is consistent with charge density analysis.

3.4. Bulk co-binder model

For practical applications, silicon anodes are often nanostructured or used in composite materials to mitigate volume expansion issues and enhance overall battery performance. Nanostructuring lithium-silicon materials is a key strategy to address challenges associated with the use of silicon-based anode material in lithium-ion batteries. Here to address one of the common approaches of the nanostructured anode with binders, we follow a combined modeling technique, MD and DFT simulation.

We performed MD calculations of bulk models for each monomer separately to determine the equilibrium density and the g(r) and then for the co-binders comparing their properties with those of the single monomer model. The average density calculated for each bulk model, the standard error, and also the number of monomers considered for single binder and co-binder configurations are tabulated in Table 3. The standard error is derived from the mean of a correlated fluctuating quantity, which fluctuates in time around an average value throughout the trajectory [49]. To gain insights into the spatial distribution of particles in the simulated system, a pair correlation function is calculated for all the binder models mentioned in Table 3.

Since we aimed to combine DFT and classical MD calculations, and considering the DFT limitation to a relatively small number of atoms, we chose a small-sized repeat unit for the polymer models. For this reason, our results on average density are significantly different from the results found in the literature. However, our values fall within the range of densities for commercially available forms of the polymer, as shown in SM: Table 3S.

We analyzed g(r) for a system composed of one type of monomer (PVA/PANI/β-PVDF/B–OH_PANI) and co-binders [SM: Figure 8S]. PANI is the system that has a smaller distance between chains and is also the system with the first peak more well-defined, showing a

1. 16 Li−Si 110
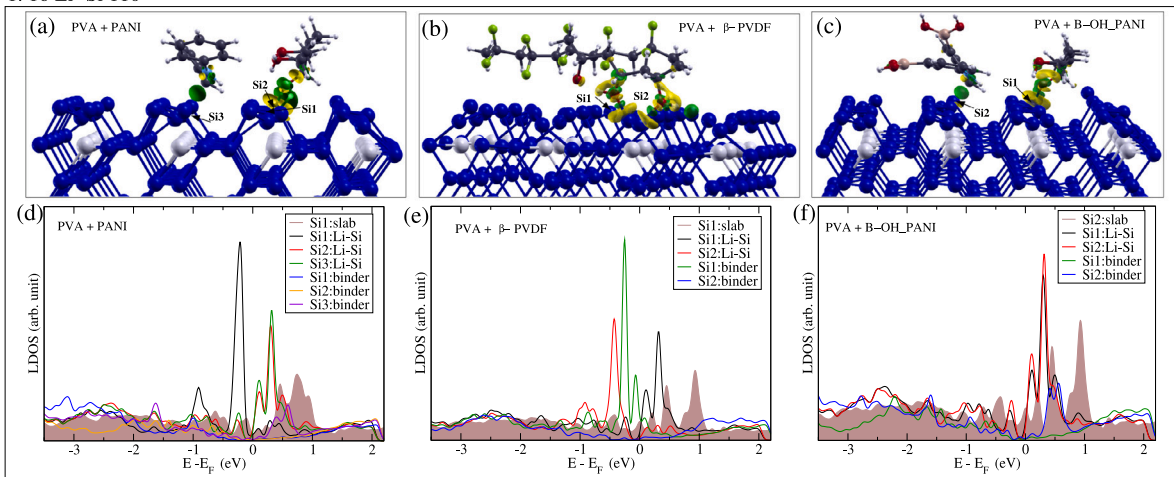
2. 20 Li−Si 111
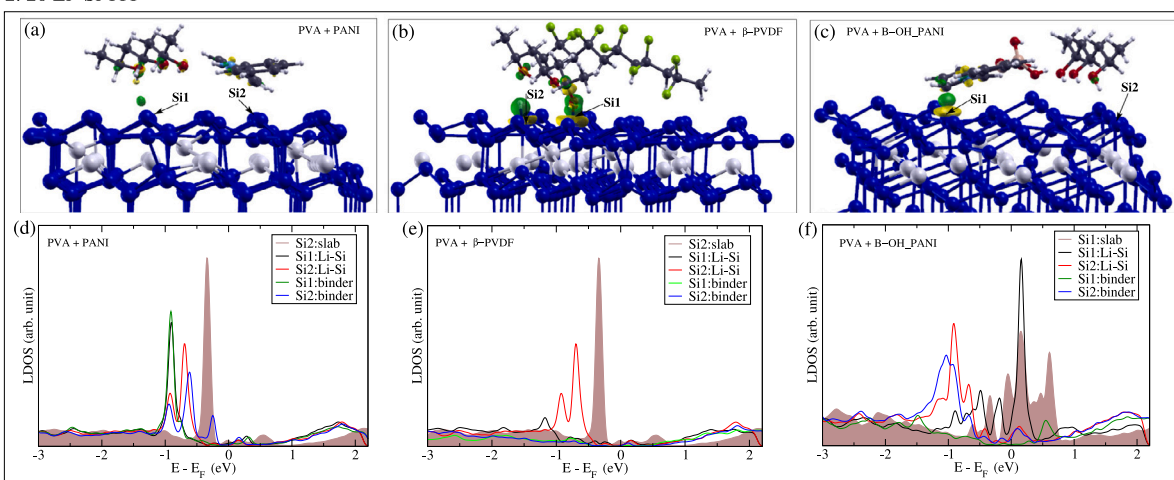
Fig. 6. 1. 16 Li–Si 110 surface in the presence of co-binders. Upper panel: charge density difference (Δρ) (a) PVA + PANI, (b) PVA + β-PVDF (c) PVA + B–OH_PANI. Lower panel: projected density of states (p-orbital) of Si sites with (d) PVA + PANI, (e) PVA + β-PVDF (f) PVA + B–OH_PANI. For all structures, the same Si sites in the absence of Li (slab), in the presence of the 16 Li (Li–Si), and the Li–Si surface with co-binder (binder) are plotted for comparison. 2. 20 Li–Si 111 surface in the presence of co-binders. Upper panel: charge density difference (Δρ) (a) PVA + PANI, (b) PVA + β-PVDF (c) PVA + B–OH_PANI. Lower panel: projected density of states (p-orbital) of Si sites with (d) PVA + PANI, (e) PVA + β-PVDF (f) PVA + B–OH_PANI. For all structures, the same Si sites in the absence of Li (slab), in the presence of the 20 Li (Li–Si), and the Li–Si surface with co-binder (binder) are plotted for comparison. In 1 & 2 (a–c), the green and yellow isosurfaces (isosurface value 0.008.) represent charge accumulation and depletion respectively. Si sites are marked accordingly as used in both panels. (For interpretation of the references to color in this figure legend, the reader is referred to the web version of this article.)

Table 3
Density and monomers considered for MD simulation of all the binders: PVA, PANI, β-PVDF, B–OH_PANI, and co-binders.

| System	Density (kg/m³)	Estimated error	Monomer numbers
PVA	1039.80	0.37	300
PANI	1074.78	0.19	300
β-PVDF	1478.34	0.40	400
B–OH_PANI	1238.75	0.17	500
PVA + PANI	1064.23	0.37	250 + 250
PVA + β-PVDF	1301.24	0.35	250 + 250
PVA + B–OH_PANI	1168.43	0.47	200 + 200

better packing of the bulk. For B–OH_PANI, PVA, and β-PVDF, the g(r) curves start increasing practically at the same point, indicating that the distances between chains are similar, the peaks are in the same position for PVA and β-PVDF, and a different position for B–OH_PANI. PVA and β-PVDF have the first peak relatively well-defined too, but both present a small shoulder in this peak. This shoulder is probably related to the fact that both molecules are not symmetric concerning the backbone, so the distances would be different depending on the molecule-molecule relative position. B–OH_PANI has the peak more

shifted towards larger values of r since the lateral substituents are bulkier (B(OH)₂ instead of H). Different intensities are related to the different number of molecules in the systems, so they are not relevant to our analysis. In the case of a co-binder system, being PVA common in each set, here pair correlation functions of the co-binder configurations are compared with their isolated counterpart. It shows that in all systems g(r) starts to increase at the same position, which is the same position as for only the PVA system, and the peak is also in the same position [SM: Figure 9S].

For studying the interactions between binders and electrode material, three different nanostructured co-binder models, as discussed in previous sections, are investigated. A supercell with two Li–Si nanostructures (modeled with Si-110 slabs and inserting Li with a ratio 1:1) of the size of 16 Å × 16 Å × 30 Å, was created. To generate an initial configuration, Li atoms are inserted in the tetrahedral positions of the Si matrix as we did with the lithiation of the sub-surface Si slab. The initial structures for the three bulk binder structures corresponding to the three co-binder combinations were obtained from a small portion of the MD snapshot which is then included in the vacuum between the two Li–Si surfaces. Finally, the simulation cell is optimized with all the atomic positions using a single k-point. All the initial and final optimized structures are shown in Fig. 7. As the lithiation process is
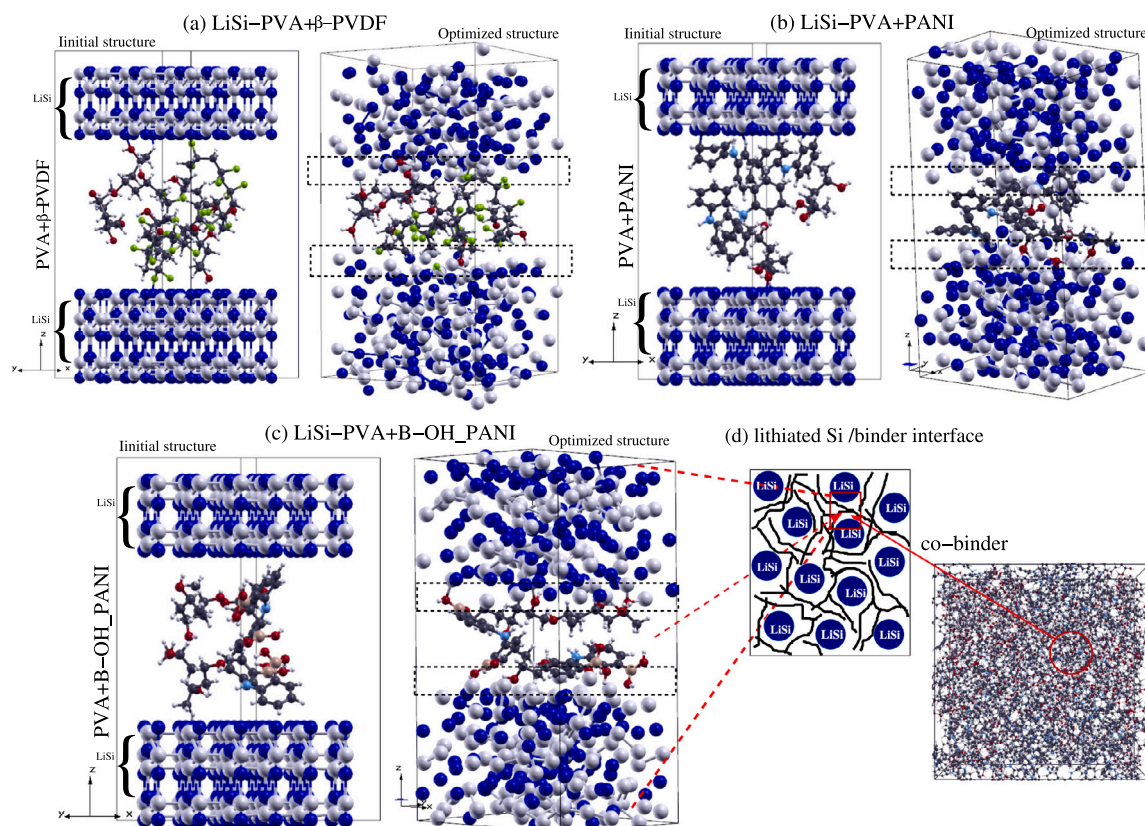
Fig. 7. Li–Si nanostructures model with initial and optimized configurations: (a) PVA+ β-PVDF bulk co-binder with 5 PVA and 3 β-PVDF molecules, (b) (a) PVA+PANI bulk co-binder with 2 PVA and 4 PANI molecules and (c) (a) PVA+B–OH_PANI bulk co binder with 3 PVA and 2 B–OH_PANI molecules. Si and Li atoms are presented with blue and gray balls respectively. (d) Schematic representation of a lithiated nanostructured Si anode-binder interface, which is correlated to the three models of our interest. MD simulated bulk binder cell is also shown here. The dashed box of (a–c) marks the interface region. (For interpretation of the references to color in this figure legend, the reader is referred to the web version of this article.)

accompanied by the amorphization of Si [50,51], one expects that the structural relaxations upon Li insertion destroy the Si crystalline coordination introducing a volume expansion as obtained here. Around the Li–Si/PVA+β-PVDF, interface [dashed box of Fig. 7(a)] bonding occurs through –OH of PVA or via strong Si–O bond formation. It also shows F–C bond breaking, leading to the release of a fluorine atom that tries to bond to Li [52–54]. This may occur due to the different chemical environments at the lithiated interface, which is not evident in our previous calculations with Li at crystalline Si subsurfaces. However, the orientations of the PVA and β-PVDF monomers are similar to those observed in Section 3.2.1. In the case of PVA+PANI, the bonding to the Li–Si system occurs through the –NH group of PANI and –OH group of PVA. In the case of PVA+B–OH_PANI, there is a crosslinking between –B(OH)$_2$ group of B–OH_PANI and –OH of PVA and this plays a strong role in the interfacial bonding. In this last case, a larger number of bonds are formed. The orientation of the –B(OH)$_2$ group towards the lithiated surface, as discussed previously (Section 3.2.1) is observed here as well.

The interface between the anode material and the binder is a critical region that can affect the stability and performance of the battery. A stable anode-binder interface ensures good electrical contact, mechanical integrity, and efficient Li-ion transport. In general, the calculation of diffusion barriers can be computationally intensive following the complexity of the interfaces. Here, we consider Li diffusion at the lowest level, looking only at the values of the formation energy of an additional Li atom across the Li–Si -binder- Li–Si interfaces in the bulkbinder model. The differences between subsequent formation energy values provide lower bounds for the diffusion barriers. The initial positions of the extra Li atom are chosen inside the voids available within the structure. The formation energy (Eq. (1)) is obtained by

optimizing the bulk-binder structures with the added Li atom located in six different positions, as shown in Fig. 8. The formation energy is a measure of how much energy is required to create that specific configuration, so a higher formation energy implies a less stable configuration. Hence, from such a configuration, it is easier, in principle, for the Li atom to come out and diffuse. Conversely, a lower formation energy suggests a more stable configuration, where the Li atom can fall inside and sit longer. Therefore, the variation in formation energy in the three bulk-binder models could be a useful indicator of different Li transport properties. Looking at Fig. 8, we can see that apart from the value at location 3 in the PVA+PVDF binder much lower than all the others, the calculated formation energies are not tremendously different. In location 3 inside PVA+PVDF, the added Li binds to closer F ions, this suggests a strong electrostatic interaction between Li and F ions within the binder matrix. Hence, the lowering in formation energy is related to the increased stability at that particular location. The trapping of Li-ion by F could be one of the reasons for the lower performance of PVDF as a binder for Si electrodes than PVA + B–OH_PANI as shown in SM [SM: Figure 10S], where the capacity retention over cycling of the single cells using PVDF and PVA+B–OH_PANI is reported. Interestingly, we can notice from Fig. 8(b) that the boronic acid functionalization of PANI decreases the formation energy of all the sites of the Li-Si - PVA+B–OH_PANI- Li–Si system compared to those of Li–Si -PVA+PANI- Li–Si. The formation energy values, in this case, are very similar all across the system, slightly higher in the binder than in the Li–Si region, which may indicate a homogeneity between the bonding environments for the Li. However, to advance any reliable conclusion on the diffusion constants and trajectories of the Li-ion, a thorough calculation of the formation energies of a three-dimensional network of sites and relative energy barriers will be necessary.
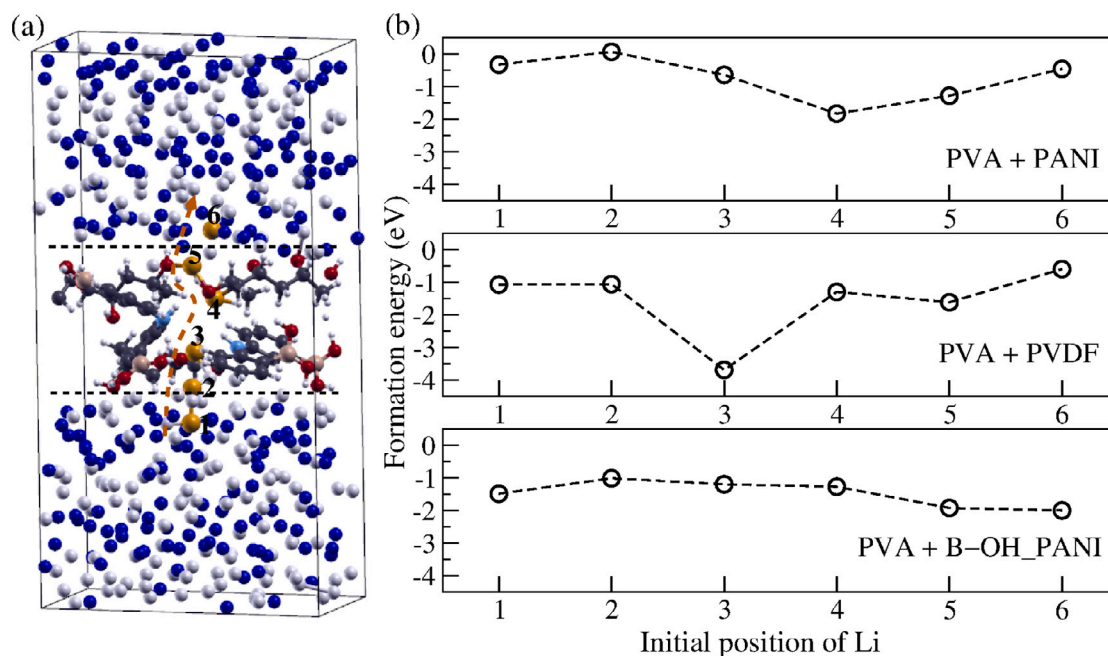
Fig. 8. (a) The initial position of Li along Li–Si -binder- Li–Si interfaces in a bulk-binder model that contains PVA + B–OH_PANI. The path is indicated by a brown dotted line. The formation energy (eV) of the added Li (brown ball) is shown for six different initial positions, which are represented by brown balls with numbers 1 to 6. (b) Formation energy values for all three bulk binder models. The black dotted line in the supercell structure (a) serves as a guide for identifying the interfaces. (For interpretation of the references to color in this figure legend, the reader is referred to the web version of this article.)

4. Conclusion

This article provides comprehensive insights into the interactions between lithiated silicon and binders in various configurations, shedding light on the stability, reactivity, and electronic properties of the Li–Si interface in the context of battery materials.

Concerning the lithiation of Si surfaces, the formation energy (E_f) is calculated to assess the stability of different Li-inserted structures. The behavior of integrated Li within the silicon matrix depends on factors such as crystal orientations, the presence of defects, and specific battery conditions. Si-110 and Si-111 facets exhibit different behaviors during lithium insertion, impacting the stability and reactivity of the system. The system becomes more stable with increasing lithium content, but the overall difference in formation energy is relatively small due to the low Li content. For Si-110, the optimized geometry with 8 Li atoms leads to elongated Si–Si bonds nearest to the Li sites, while with 24 Li, more Si–Si bonds get elongated. For Si-111, even with a small number of Li atoms, the Si–Si bonds at the surface mostly elongate, and with 20 and 30 Li atoms, surface reconstruction occurs, impacting stability and reactivity. Distortion of the Si network upon lithiation and the formation of different Si–Li alloys are evident, supporting the importance of understanding these reconstructions for predicting binding mechanisms.

Adsorption of binders on Li-inserted silicon surfaces is crucial, especially for high-capacity materials like silicon with significant volume changes during cycling. Adsorption energy is calculated to assess the strength of binder adhesion on lithiated Si surfaces. Co-binding of polymers with PVA is explored for both the lithiated Si facets, and the adsorption energy is compared with that of single binders. Lithium insertion weakens adhesion, but co-binding helps in stabilizing additional monomers on the surface. Actually, co-binding, compared to single bindings, enhances the adsorption energy and contributes to better adhesion properties. The stability and reactivity of the lithiated-silicon interface with the binder are influenced by the nature of binder adsorption, which varies with lithium content and silicon facet orientation. Comprehensive insights into the electronic structure of the interface are gained through charge density analysis and projected density of states performed on co-binder configurations. The interplay of co-binder composition, silicon facet orientation, and lithium content significantly influences charge distribution and electronic states at the interface.

Charge transfer at the interface is observed impacting the local coordination and electronic structure of the outmost Si atoms. Co-binding leads to a reduction of unsaturated Si and in Löwdin charges for different Li content. Finally, molecular dynamics simulations are used to study nanostructured co-binder models between two Li–Si slabs. Here we use the MD simulation to create a realistic polymer for a full coverage of the surface. The pair correlation function (g(r)) is calculated for single binders and co-binder configurations, revealing spatial distribution and interaction strengths. Co-binding does not significantly influence the polymer-polymer distance, and the form of the g(r) curves remains similar for most systems.

Finally, we have analyzed the formation energy of a Li atom along an ideal path through the Si slab-binders-Si slab interface. The relationship between the formation energy and diffusion barrier is not always straightforward. This is because diffusion is affected by a range of factors, such as the thermodynamics, kinetics, and atomic motion involved in finding the path of minimum energy and transition states. Therefore, investigating the diffusion behavior of lithium-ion at the anode-binder interface will be a future aspect of this work.

CRediT authorship contribution statement

Rita Maji: Writing – original draft, Investigation, Formal analysis, Data curation. **Michele A. Salvador:** Writing – review & editing, Methodology. **Alice Ruini:** Writing – review & editing, Supervision, Funding acquisition. **Rita Magri:** Writing – review & editing, Supervision, Funding acquisition. **Omer Suat Taskin:** Validation. **Neslihan Yuca:** Validation. **Elena Degoli:** Funding acquisition, Writing – review & editing, Supervision.

Declaration of competing interest

The authors declare that there are no conflicts of interest regarding the publication of this paper.

Data availability

The data that has been used is confidential.

Appendix A. Supplementary data

Supplementary material related to this article can be found online at https://doi.org/10.1016/j.jpowsour.2024.234705.

References

[1] K. Feng, M. Li, W. Liu, A.G. Kashkooli, X. Xiao, M. Cai, Z. Chen, Silicon-based anodes for lithium-ion batteries: From fundamentals to practical applications, Small 14 (2018) 1702737.
[2] Alba Franco Gonzalez, Nai-Hsuan Yang, Ru-Shi Liu, Silicon anode design for lithium-ion batteries: Progress and perspectives, J. Phys. Chem. C 121 (50) (2017) 27775–27787.
[3] Y. Jin, B. Zhu, Z. Lu, N. Liu, J. Zhu, Challenges and recent progress in the development of Si anodes for lithium-ion battery, Adv. Energy Mater. 7 (2017) 1700715.
[4] Shenggong He, Shimin Huang, Shaofeng Wang, Isao Mizota, Xiang Liu, Xianhua Hou, Considering critical factors of silicon/graphite anode materials for practical high-energy lithium-ion battery applications, Energy Fuels 35 (2) (2021) 944–964.
[5] S. Chae, S.-H. Choi, N. Kim, J. Sung, J. Cho, Integration of graphite and silicon anodes for the commercialization of high-energy lithium-ion batteries, Angew. Chem. Int. Edn 59 (2020) 110.
[6] Li Haodong, Li Haoyu, Lai Yizhu, Yang Zhiwei, Yang Qing, Liu Yang, Zheng Zhuo, Liu Yuxia, Sun Yan, Zhong Benhe, Wu Zhenguo, Guo Xiaodong, Revisiting the preparation progress of nano-structured Si anodes toward industrial application from the perspective of cost and scalability, Adv. Energy Mater. 12 (7) (2022) 2102181.
[7] C. Wang, H. Wu, Z. Chen, M.T. McDowell, Y. Cui, Z. Bao, Self-healing chemistry enables the stable operation of silicon microparticle anodes for high-energy lithium-ion batteries, Nature Chem. 5 (2013) 1042.
[8] D. Chen, D. Wang, Y. Yang, Q. Huang, S. Zhu, Z. Zheng, Self-healing materials for next-generation energy harvesting and storage devices, Adv. Energy Mater. 7 (23) (2017) 1700890.
[9] Yunsong Li, Kevin Leung, Yue Qi, Computational exploration of the Li-electrode|electrolyte interface in the presence of a nanometer thick solid-electrolyte interphase layer, Acc. Chem. Res. Nanoelectrochem. 49 (2016) 2363–2370.
[10] Satu Kristiina Heiskanen, Jongjung Kim, Brett L. Lucht, Generation and evolution of the solid electrolyte interphase of lithium-ion batteries, Joule 3 (10) (2019) 2322–2333.
[11] N. Yuca, I. Kalafat, E. Guney, B. Cetin, O.S. Taskin, Self-healing systems in silicon anodes for Li-ion batteries, Materials 15 (2022) 2392.
[12] Aiping Wang, Sanket Kadam, Hong Li, Siqi Shi, Yue Qi, Review on modeling of the anode solid electrolyte interphase (SEI) for lithium-ion batteries, NPJ Comput. Mater. 15 (2018).
[13] Andrea Miranda, Kasturi Sarang, Bolormaa Gendensuren, Eun-Suok Oh, Jodie Lutkenhaus, Rafael Verduzco, Molecular design principles for polymeric binders in silicon anodes, Mol. Syst. Des. Eng. 5 (2020) 709.
[14] Zeeshan Ahmad, Victor Venturi, Hasnain Hafiz, Venkatasubramanian Viswanathan, Interfaces in solid electrolyte interphase: Implications for lithium-ion batteries, J. Phys. Chem. C 125 (2021) 11301–11309.
[15] Lorena Alzate-Vargas, Samuel M. Blau, Evan Walter Clark Spotte-Smith, Srikanth Allu, Kristin A. Persson, Jean-Luc Fattebert, Insight into SEI growth in Li-ion batteries using MoleculNeslihan yucaar dynamics and accelerated chemical reactions, J. Phys. Chem. C 125 (2021) 18588–18596.
[16] Wei Wang, Prashant N. Kumta, Reversible high capacity nanocomposite anodes of Si/C/SWNTs for rechargeable Li-ion batteries, J. Power Sources 2 (172) (2007) 650–658.
[17] W.-J. Zhang, A review of the electrochemical performance of alloy anodes for lithium-ion batteries, J. Power Sources 196 (2011) 13–24.
[18] Thomas M. Higgins, Sang-Hoon Park, Paul J. King, Chuanfang (John) Zhang, Niall McEvoy, Nina C. Berner, Dermot Daly, Aleksey Shmeliov, Umar Khan, Georg Duesberg, Valeria Nicolosi, Jonathan N. Coleman, A commercial conducting polymer as both binder and conductive additive for silicon nanoparticle-based lithium-ion battery negative electrodes, ACS Nano 10 (3) (2016) 3702–3713.
[19] Qiu He, Bin Yu, Zhaohuai Li, Yan Zhao, Density functional theory for battery materials, Energy Environ. Mater. 2 (2019) 264–279.
[20] H. Euchner, A. Groß, Atomistic modeling of Li- and post-Li-ion batteries, Phys. Rev. Mater. 6 (2022) 040302.
[21] A.J. Fragoso-Medina, R.G. Escobedo-González, M.I. Nicolás-Vázquez, G.A. Arroyo-Razo, M.O. Noguez-Córdova, R. Miranda-Ruvalcaba, A DFT study of the geometrical, spectroscopical and reactivity properties of diindolylmethane-phenylboronic acid hybrids, Molecules 22 (10) (2017) 1744.
[22] Eduardo C. Escudero-Adán, Antonio Bauzá, Claude Lecomte, Antonio Frontera, Pablo Ballester, Boron triel bonding: a weak electrostatic interaction lacking electron-density descriptors, Phys. Chem. Chem. Phys. 20 (2018) 24192.
[23] R. Maji, M.A. Salvador, A. Ruini, R. Magri, E. Degoli, A first-principles study of self-healing binders for next-generation si-based lithium-ion batteries, Mater. Today Chem. 29 (2023) 101474.
[24] Hongwei Mi, Fang Li, Chuanxin He, Xiaoyan Chai, Qianling Zhang, Cuihua Li, Yongliang Li, Jianhong Liu, Three-dimensional network structure of silicon-graphene-polyaniline composites as high performance anodes for lithium-ion batteries, Electrochim. Acta 190 (2016) 1032–1040.
[25] K. Bicy, Amadou Belal Gueye, Didier Rouxel, Nandakumar Kalarikkal, Sabu Thomas, Lithium-ion battery separators based on electrospun PVDF: A review, Surf. Interfaces 31 (2022) 101977.
[26] P. Giannozzi, Stefano Baroni, Nicola Bonini, Matteo Calandra, Roberto Car, Carlo Cavazzoni, Davide Ceresoli, Guido L. Chiarotti, Matteo Cococcioni, Ismaila Dabo, et al., QUANTUM ESPRESSO: a modular and open-source software project for quantum simulations of materials, J. Phys.: Condens. Matter. 21 (2009) 395502.
[27] D.R. Hamann, Optimized norm-conserving Vanderbilt pseudopotentials, Phys. Rev. B 88 (8) (2013).
[28] J.P. Perdew, K. Burke, M. Ernzerhof, Generalized gradient approximation made simple, Phys. Rev. Lett. 77 (1996) 3865–3868.
[29] R. Fletcher, Practical Methods of Optimization, Wiley, New York, 1987.
[30] S. Grimme, Semiempirical GGA-type density functional constructed with a long-range dispersion correction, J. Comput. Chem. 27 (2006) 1787–1799.
[31] D. van der Spoel, E. Lindahl, B. Hess, G. Groenhof, A.E. Mark, H.J.C. Berendsen, GROMACS: Fast, flexible and free, J. Comput. Chem. 26 (2005) 1701–1719.
[32] Frank Neese, The ORCA program system, WIREs Comput. Mol. Sci. 2 (2012) 73–78.
[33] Frank Neese, Software update: the ORCA program system, version 4.0, WIREs Comput. Mol. Sci. 8 (2018) e1327.
[34] Axel D. Becke, A new mixing of Hartree–Fock and local density-functional theories, J. Chem. Phys. 98 (2) (1993) 1372–1377.
[35] R. Krishnan, J.S. Binkley, R. Seeger, J.A. Pople, Self-consistent molecular orbital methods. XX. A basis set for correlated wave functions, J. Chem. Phys. 72 (1980) 650–654.
[36] S. Grimme, S. Ehrlich, L. Goerigk, J comput chem, effect of the damping function in dispersion corrected density functional theory, J. Comput. Chem. 32 (7) (2011) 1456–1465.
[37] S. Grimme, J. Antony, S. Ehrlich, H. Krieg, A consistent and accurate ab initio parametrization of density functional dispersion correction (DFT-D) for the 94 elements H-Pu, J. Chem. Phys. 132 (15) (2010) 154104, 21.
[38] C.M. Breneman, K.B. Wiberg, Determining atom-centered monopoles from molecular electrostatic potentials. The need for high sampling density in formamide conformational analysis, J. Comput. Chem. 11 (1990) 361–373.

[39] W.L. Jorgensen, D.S. Maxwell, J. Tirado-Rives, Development and testing of the OPLS all- atom force field on conformational energetics and properties of organic liquids, J. Am. Chem. Soc. 118 (1996) 11225–11236.

[40] B. Kurt, H. Temel, Development of AMBER parameters for molecular dynamics simulations of boron compounds containing aromatic structure, Chem. Phys. Lett. 775 (2021) 138656.

[41] R.W. Hockney, S.P. Goel, J. Eastwood, Quiet high resolution computer models of a plasma, J. Comput. Phys. 14 (1974) 148–158.

[42] G. Bussi, D. Donadio, M. Parrinello, Canonical sampling through velocity rescaling, J. Chem. Phys. 126 (2007) 014101.

[43] H.J.C. Berendsen, J.P.M. Postma, A. Di Nola, J.R. Haak, Molecular dynamics with coupling to an external bath, J. Chem. Phys. 81 (1984) 3684–3690.

[44] M. Parrinello, A. Rahman, Polymorphic transitions in single crystals: A new molecular dynamics method, J. Appl. Phys. 52 (1981) 7182–7190.

[45] Maria K.Y. Chan, C. Wolverton, Jeffrey P. Greeley, First principles simulations of the electrochemical lithiation and delithiation of faceted crystalline silicon, J. Am. Chem. Soc. 134 (2012) 14362–14374.

[46] Georgios A. Tritsaris, Efthimios Kaxiras, Sheng Meng, Enge Wang, Adsorption and diffusion of lithium on layered silicon for Li-ion storage, Nano Lett. 13 (5) (2013) 2258–2263.

[47] Hyunwoo Kim, Kyoung Eun Kweon, Chia-Yun Chou, John G. Ekerdt, Gyeong S. Hwang, On the nature and behavior of Li atoms in Si: A first principles study, J. Phys. Chem. C 114 (41) (2010) 17942–17946.

[48] B. Gao, S. Sinha, L. Fleming, O. Zhou, Alloy formation in nanostructured silicon, Adv. Mater. 13 (2001) 816.

[49] Berk Hess, Determining the shear viscosity of model liquids from molecular dynamics simulations, J. Chem. Phys. 116 (2002) 209.

[50] Hyunwoo Kim, Chia-Yun Chou, John G. Ekerdt, Gyeong S. Hwang, Structure and properties of Li-Si alloys: A first-principles study, J. Phys. Chem. C 115 (5) (2011) 2514–2521.

[51] Sung Chul Jung, Young-Kyu Han, Ab initio molecular dynamics simulation of lithiation-induced phase-transition of crystalline silicon, Electrochim. Acta 62 (2012) 73–76.

[52] Jeffrey Read, Evan Collins, Brandon Piekarski, Sheng Zhang, LiF formation and cathode swelling in the Li/CFx battery, J. Electrochem. Soc. 158 (2011) A504.

[53] Binghong Han, Maria Jose Piernas-Muñoz, Fulya Dogan, Joseph Kubal, Stephen E. Trask, Ira D. Bloom, John T. Vaughey, Baris Key, Probing the reaction between PVDF and LiPAA vs Li7Si3: Investigation of binder stability for Si anodes, J. Electrochem. Soc. 166 (2019) 12.

[54] Ni Jie, Yike Lei, Yongkang Han, Yingchuan Zhang, Cunman Zhang, Zhen Geng, Qiangfeng Xiao, Prefabrication of a lithium fluoride interfacial layer to enable dendrite-free lithium deposition, Batteries 9 (5) (2023) 283.